Nuclear Science and Techniques (2026) 37:96
https://doi.org/10.1007/s41365-026-01920-7

Performance of high-resolution PET detectors based on long semi-monolithic scintillator slabs

Samuel Mungai Kinyanjui[1,2] · Zhonghua Kuang[1,3] · Zheng Liu[1] · Ning Ren[1] · Yongfeng Yang[1]

Received: 2 July 2024 / Revised: 29 November 2024 / Accepted: 6 December 2024 / Published online: 21 March 2026

Abstract
Conventional positron emission tomography (PET) scanners use either highly segmented or monolithic scintillator detectors. Depth of interaction (DOI) information is vital for high-resolution PET scanners that use either segmented scintillator detectors with a large crystal-length-to-width aspect ratio or monolithic scintillator detectors with a large crystal-thickness-to-spatial-resolution ratio. Semi-monolithic scintillator detectors maintain the intrinsic DOI-encoding capability of monolithic detectors, but with a substantially smaller edge effect. The objective of this study was to compare the performance of semi-monolithic scintillator detectors with different slab thicknesses, slab surface treatments, and reflector types. Four long semi-monolithic detectors consisting of lutetium yttrium oxyorthosilicate (LYSO) slabs of 0.96 mm × 56 mm × 10 mm and 0.81 mm × 56 mm × 10 mm, with and without black paint on both the end and front surfaces, were measured. In addition, semi-monolithic detectors using either barium sulfate ($BaSO_4$) or an enhanced specular reflector (ESR) as the inter-slab reflector were compared for the first time. The semi-monolithic detectors were read out by a 4 × 16 silicon photomultiplier array with a row and column summing readout circuit, and the signals were processed using electronics developed in our laboratory. Black paint treatment of the two end and front surfaces degraded the energy resolution but improved both the spatial resolution in the monolithic direction and DOI resolution, thereby improving the overall detector performance. The detector using an ESR reflector provided clearer individual slab identification in the flood histogram and a similar spatial resolution in the monolithic direction, DOI resolution, and energy resolution. The squared centroid of gravity (COG) method improved the spatial resolution in the monolithic direction by ~30% compared with the COG method. The long semi-monolithic scintillator detectors optimized in this work provide clear identification of LYSO slabs of 0.96 and 0.81 mm thick, a spatial resolution in the monolithic direction of ~1.7 ± 0.3 mm, a DOI resolution of ~2.1 ± 0.7 mm, and an energy resolution of ~17.5 ± 2.0%. These detectors can be used to develop high-performance small-animal and organ-specific PET scanners.

Keywords Positron emission tomography (PET) · PET detector · Semi-monolithic scintillator · Silicon photomultiplier · Depth of interaction

1 Introduction

Positron emission tomography (PET) is a non-invasive medical imaging tool that is used for the early detection of many major diseases such as cancer [1, 2]. Achieving a high spatial resolution in a PET scanner allows for the accurate measurement of biochemical processes in the organs and tissues of living subjects by reducing the partial volume effect [3]. This is particularly important for small-animal imaging [4–6] and clinical applications such as neuroimaging [7].

The depth of interaction (DOI) uncertainty reduces the spatial resolution of PET scanners, particularly for small-animal and organ-specific PET scanners that use detectors

Samuel Mungai Kinyanjui and Zhong-Hua Kuang have contributed equally to this work.

This work was supported in part by the National Natural Science Foundation of China (Nos. 62101539 and 12375358), the Basic Research Program of Shenzhen (No. JCYJ20220818101612027), the Natural Science Foundation of Hunan Province (No. 2024JJ6414), the Key Laboratory of Biomedical Imaging Science and System, Chinese Academy of Sciences, and the Key Laboratory for Magnetic Resonance and Multimodality Imaging of Guangdong Province (No. 2023B1212060052).

Extended author information available on the last page of the article

with a high crystal-length-to-width aspect ratio [6, 8]. Owing to crystal penetration, events may be incorrectly assigned to the incorrect line of response when detectors that lack DOI measurements or have poor DOI resolution are used. The error resulting from DOI uncertainty increases as the aspect ratio of the crystal increases. In the most common cylindrical detector geometry, the DOI uncertainty error increases with both the radial offset and ring difference. DOI encoding in PET detectors is important for achieving a uniformly high spatial resolution.

At present, state-of-the-art PET scanners use either pixelated or monolithic scintillator crystals that are read out by silicon photomultiplier (SiPM) photodetectors. Pixelated detectors can achieve a high timing resolution because the scintillation photons are constrained in a smaller area and the photodetector can achieve a high signal-to-noise ratio. They can also achieve superior planar position resolution using small scintillator crystals [9, 10]. However, DOI information is not intrinsically present in pixelated detectors, and modified detector designs, such as dual-ended readout or multiple-layer crystals, are required to measure the DOI, which increases the cost and complexity of the detectors [11–15]. Pixelated detectors also have a lower detection efficiency owing to the dead space occupied by the inter-crystal reflectors [5]. In monolithic scintillator detectors, the DOI information is intrinsically presented, as it can be extracted from the scintillation photon distribution [5, 7]. The efficiency of monolithic detectors is superior and their cost is lower compared with pixelated detectors. However, monolithic detectors exhibit the disadvantage of large edge effects. Owing to the loss and reflection of scintillation photons at the edge of the detector, fewer scintillation photons are detected and the measured planar positions are compressed for the interactions occurring close to the edge of the detector, resulting in degradation of both the planar and DOI resolutions. Both the planar spatial and DOI resolutions deteriorate and the edge effect increases as the detector thickness increases [16–23].

Semi-monolithic scintillator detectors exploit the advantages of both pixelated and monolithic scintillator detectors. They maintain the inherent DOI-encoding capability, although the scintillation photon distribution is limited to fewer photosensors along the monolithic direction. Semi-monolithic detectors have a smaller edge effect compared with monolithic detectors, which can be further reduced using longer scintillator slabs. Semi-monolithic scintillator PET detectors were proposed and preliminarily evaluated by Chung et al. [24, 25] around 2010 using detectors consisting of one or more scintillator slabs. Later, least-squares minimization and maximum likelihood positioning algorithms were developed [26] and slab surface treatments were optimized [27, 28] by our group for semi-monolithic detectors. In recent years, more studies have been conducted on the development of semi-monolithic detectors for small animal [29], dedicated brain, and whole-body [30–32] PET scanners. It has also been demonstrated that machine-learning-based positioning algorithms can improve both the spatial resolution in the monolithic direction and the DOI resolution, as well as reduce the edge effect [32–34].

In this study, four semi-monolithic detectors using long lutetium–yttrium oxyorthosilicate (LYSO) slab arrays with different slab surface treatments, slab thicknesses, and inter-slab reflectors were evaluated. The performances of a semi-monolithic detector using two different inter-slab reflectors were compared for the first time. The positioning resolutions in the monolithic direction obtained using the conventional centroid of gravity (COG) and squared COG algorithms were also compared.

2 Materials and methods

2.1 Detector modules

Figure 1 shows a schematic of the detector module. The detector module was composed of LYSO slabs that were read out by a SiPM array with a lightguide between them. Table 1 shows the detailed parameters of the four detector modules used in this study. The semi-monolithic LYSO arrays were manufactured by Epic Crystal Co. (Shanghai, China). The reflector between the individual slabs of detectors 1, 2, and 4 was barium sulfate ($BaSO_4$), whereas the enhanced specular reflector (ESR) of 3 M Company was used in detector 3. The thickness of the $BaSO_4$ and that of the ESR plus optical glue were both 0.08 mm. The optical glue used was EPO-TEK 301 (EXPOXY Technology INC., MA, USA). The two end and front surfaces of detectors 1, 3, and 4 were unpolished and painted with a black marker pen, whereas the surfaces of detector 2 were unpolished and left unpainted. For all detectors, the two large surfaces of

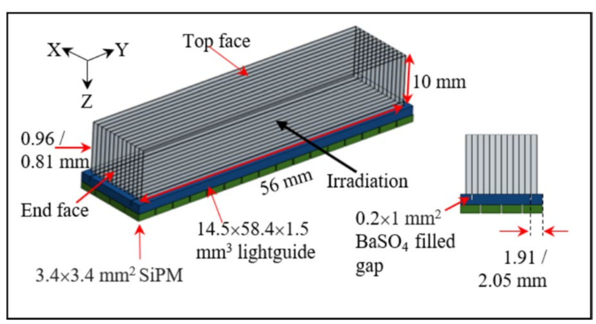

Fig. 1 (Color online) Schematic of the detector module showing the dimensions of all components. The detector module was composed of 12 or 14 thin LYSO scintillator slabs separated by reflectors and read out by a SiPM array

Table 1 Parameters of the four distinct detectors used in this work

Detector No.	No. of slabs	Size of slabs (mm^3)	Front and end surface treatment	Inter-slab reflector
1	12	$0.96 \times 56 \times 10$	Painted	$BaSO_4$
2	12	$0.96 \times 56 \times 10$	Unpainted	$BaSO_4$
3	12	$0.96 \times 56 \times 10$	Painted	ESR
4	14	$0.81 \times 56 \times 10$	Painted	$BaSO_4$

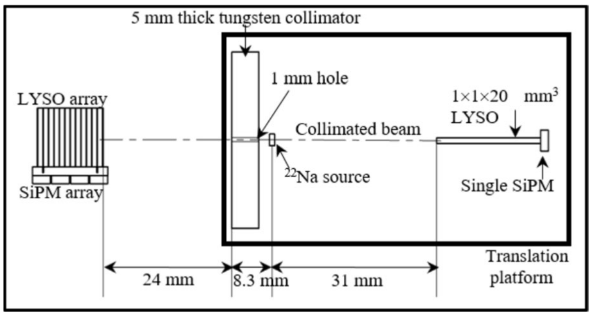

Fig. 2 (Color online) Experimental setup for the coincidence measurements

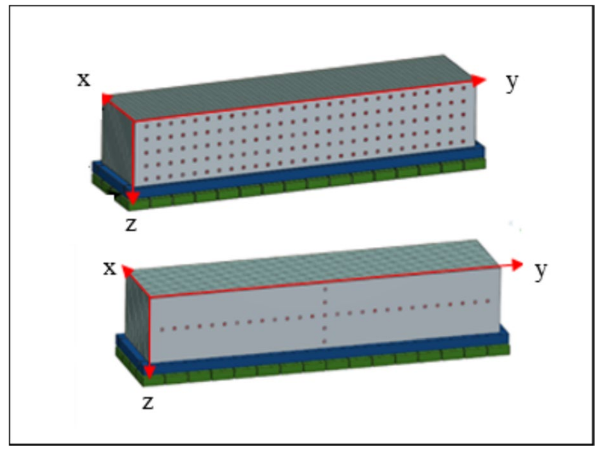

Fig. 3 (Color online) Irradiation positions for (top) detectors 1 and 4, and (bottom) detectors 2 and 3

each slab and the bottom surface interfacing with the readout SiPM were polished. Each detector module was read out by a 4×16 SiPM array coupled to the bottom of the LYSO array. The SiPM array consisted of 64 single SiPM pixels (S14160-3050HS; Hamamatsu Inc., Hamamatsu, Japan). Each single SiPM had a size of 3.4 mm × 3.4 mm and an active area of 3 mm × 3 mm. The pitch of the SiPM array was 3.65 mm. All measurements were performed at a SiPM bias voltage of 44.5V. The lightguide was made of 1.5 mm-thick k9 glass with a refractive index of 1.51.

To enhance slab identification, two edge grooves, 0.2 mm wide and 1 mm deep, were cut into the lightguide. The grooves were filled with the $BaSO_4$ reflector. For detectors 1 to 3, the grooves were 1.91 mm from both edges. For detector 4, the grooves were 2.05 mm from both edges. Optical grease with a refractive index of 1.41 was used between both the lightguide and scintillator slab array and the lightguide and SiPM array.

2.2 Experimental setup

The experimental setup is illustrated in Fig. 2. All measurements were conducted in a light-tight plastic chamber covered with a black cloth, and the operating temperature of the detectors was 14 °C. The flood histogram was measured by placing a 0.3 mm-diameter ^{22}Na point source with an activity of 165 kBq 4 mm from one lateral face of the detector. Monolithic direction spatial, DOI, and energy resolution measurements were performed in coincidence with a reference detector. The reference detector was a single LYSO crystal of 1 mm × 1 mm × 20 mm wrapped with Teflon and read out by a single Hamamatsu S14160-3050HS SiPM with an active area of 3 mm × 3 mm. A collimated 511 keV beam was produced by placing the ^{22}Na point source between the reference detector and a 5 mm-thick tungsten collimator with a 1 mm-diameter drilled hole. The 1 mm hole of the collimator, ^{22}Na point source, and reference detector were well aligned and placed on a motorized translational platform. The semi-monolithic detector was placed on a stationary platform. The translational platform could move in both the monolithic direction (y-axis) and DOI direction (z-axis spanning from the top of the detector to the SiPM array). The semi-monolithic scintillator detector was irradiated from a series of (y, z) positions by moving the translational platform. As shown in the top part of Fig. 3, detectors 1 and 4 were irradiated at 27×5 positions starting 2 mm from one end and 1 mm from the front, with a stepping size of 2 mm in both the monolithic and DOI directions. To reduce the measurement time, detectors 2 and 3 were irradiated only at 27 y positions along the center z and five z positions along the middle y, as shown in the bottom part of Fig. 3, and only the results from these positions were used to compare the performances of the four detectors. The irradiation time for each position was 2200 s. The percentage of useful coincidence events relative to the total number of single events was

~0.02% for an energy window of 350 – 650 keV for both detectors.

2.3 Electronics and data acquisition

The 64 signals from the SiPM array were aggregated by a row-column summing circuit to form four row and 16 column signals, as shown in Fig. 4. The four row signals were used for slab identification (x), whereas the 16 column signals were used for both the y- and z-position measurements.

The 20 signals were propagated to a pre-amplifier board, where all of the signals were first amplified using voltage feedback amplifiers (model AD8056, Analog Devices, MA, USA). A timing signal was produced by summing the four pre-amplified row signals. The timing signal was amplified using a fast amplifier (model AD8045; Analog Devices, MA, USA). A 50 mV threshold signal was used together with the timing signal to generate three differential timing signal pairs using three high-speed comparators (model ADCMP604; Analog Devices, MA, USA).

The three differential timing signal pairs and 20 energy signals of the test detector, as well as one differential timing signal pair and one energy signal of the reference detector, were propagated using micro-coaxial cables to a singles processing unit (SPU) originally developed for our SIAT bPET scanner [35], as shown in Fig. 5. The SPU board could process eight independent dual-ended readout detectors, each containing eight energies and one differential timing signal pair. Three and one SPU electronics blocks were used to read out the test and reference detectors, respectively.

In the SPU, the energy signals from the pre-amplifier boards were first shaped and amplified. Second, the waveforms of the energy signals were sampled at a rate of 62.5 MHz using analog-to-digital converters (ADCs). Third, the digital signals were processed in a field-programmable gate array (FPGA) to determine the signal energies by calculating the areas under the waveforms. This was achieved by summing 18 waveform samples and subtracting the baseline, which was the average of four samples obtained before the rising edge of the waveform. For each electronics block, a differential timing pair was sent to a tapped delay line time-to-digital converter (TDC) to obtain the timestamp of the event, which was also used as the starting signal for the area calculation of the energy. Finally, from each SPU electronics block, eight energy values and a timestamp for each event were sent to the host PC using an Ethernet-based user datagram protocol (UDP) [36–39].

Software-based data selection and coincidence processing were carried out on the host PC. A coincidence timing window of 10ns was used. The coincidence data containing 20 energies of the test detector and the time difference between the reference and test detectors were stored as list-mode data and used for further analysis.

2.4 Data analysis

2.4.1 Planar position

The (x) and (y) coordinates of the interaction were calculated using the conventional COG algorithm, as follows:

$$x = \frac{\sum_{j=1}^{4} j \times q_j}{5\sum_{j=1}^{4} q_j}, \tag{1}$$

$$y = \frac{\sum_{i=1}^{16} i \times q_i}{17\sum_{i=1}^{16} q_i}. \tag{2}$$

The (y) coordinate was also calculated using the squared COG algorithm, as follows:

$$y = \frac{\sum_{i=1}^{16} i \times q_i^2}{17\sum_{i=1}^{16} q_i^2}, \tag{3}$$

where i is the column number of the signals and q_i is the amplitude of the i-th column signal. j is the row number of the signals and q_j is the amplitude of the j-th row signal. From the calculated (x, y) coordinates, a flood histogram

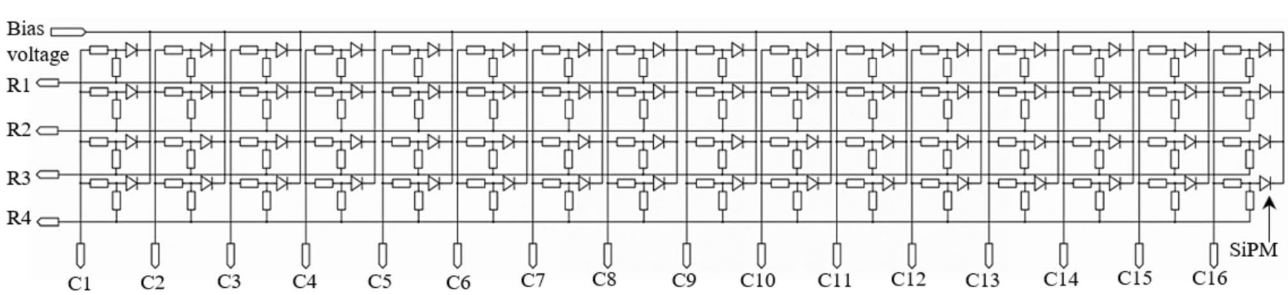

Fig. 4 Row-column resistor network readout circuit of the 4×16 SiPM array. R represents the rows and C represents the columns. All resistors were 200 Ω

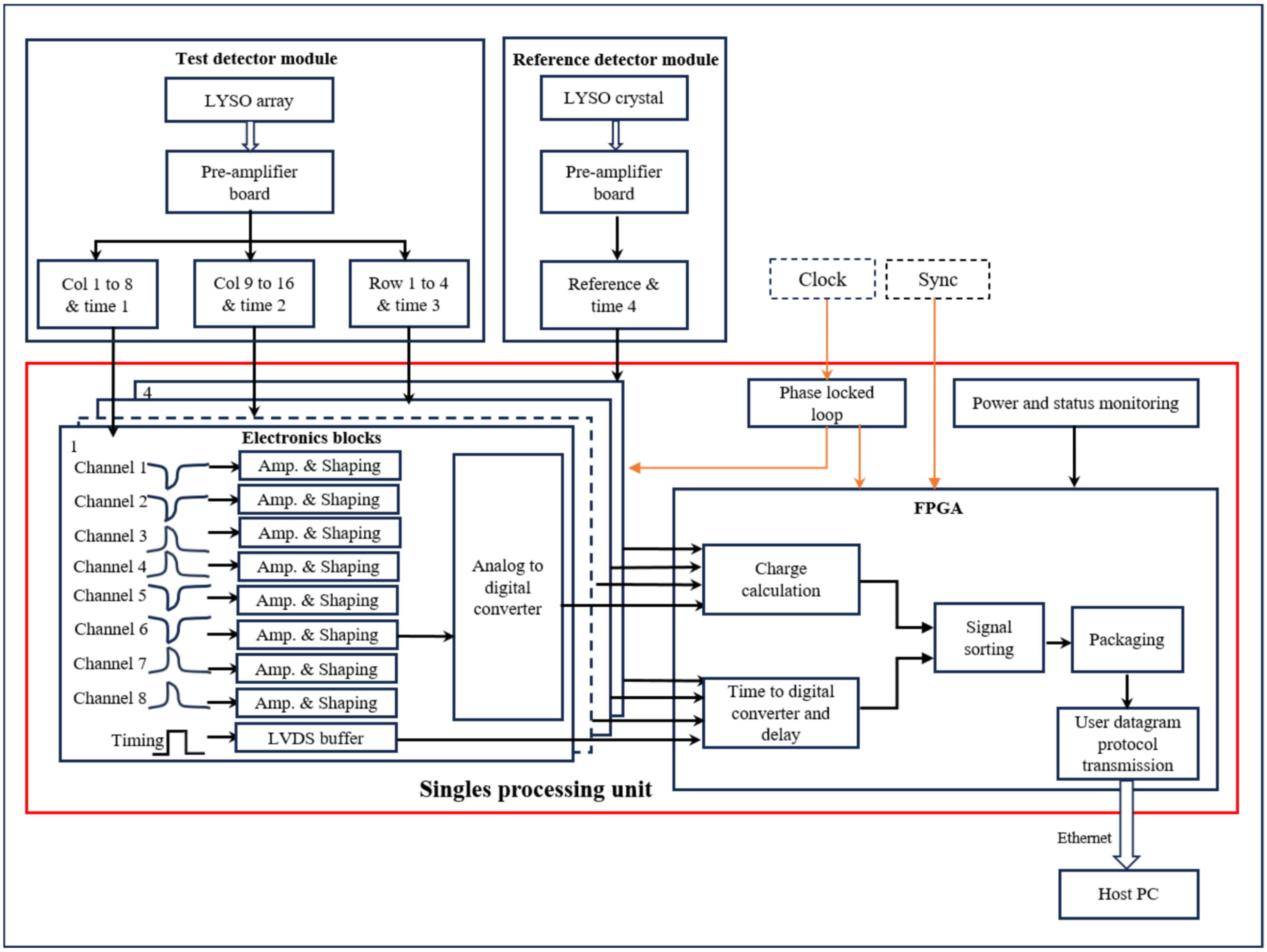

Fig. 5 (Color online) Schematic of the signal processing electronics system

showing the 2D distribution of the gamma interaction positions in the detector was plotted to demonstrate the slab identification of the detector. The flood histogram could be segmented to obtain a slab lookup table that could later be used to assign events to different slabs. For the coincidence measurement of the irradiation of a specific (y, z) position of the detector, histograms of y coordinates could be obtained for individual slabs using either the COG or squared COG Algorithm [40]. The histograms were fitted using a Gaussian function to obtain the peak positions. For each (y, z) position, the peak position of the y histograms was determined as the average of all slabs. The curve of the peak positions and true y irradiation position values for a specific z was fitted using a cubic polynomial function to obtain the fitting parameters. The measured y histogram of each (y, z) position could be converted from the pixel value into mm using the fitting parameters. The converted y histograms were then fitted using Gaussian functions, and the FWHM y resolutions were obtained for all measured positions.

2.4.2 Energy

The detector energy was calculated by summing the amplitudes of the 16 column signals. The energy histograms for each irradiation position were populated for all individual slabs. Gaussian fitting was performed and the energy resolution was calculated as the ratio of the FWHM to the mean.

2.4.3 DOI

The DOI of the gamma interaction was estimated using the inverse standard deviation of the amplitudes of the 16 column signals, as shown in Eq. (4):

$$\mathrm{DOI} = \frac{1}{\sqrt{\frac{1}{16}\sum_{i=1}^{16}\left(q_{ni} - \bar{q}_n\right)^2}}, \tag{4}$$

where q_{ni} is the normalized amplitude of the i-th column signal and $\bar{q}_n$ is the average amplitude of the 16 column signals. Five DOI histograms of each *y* position were obtained for each slab, and Gaussian fitting was performed to obtain the FWHMs and peak positions of the histograms. The FWHM was converted into mm using the peak positions of the neighboring DOI histograms and the known DOI interval of 2 mm. An energy window of 350 – 650 keV was used for all results in this work. The irradiation beam width, which was estimated to be ~1 mm, was not subtracted from the *y* and DOI resolutions.

2.4.4 Timing

The timing of the detector was defined as the timing difference between the reference and test detectors. The timing spectra of each irradiation position were populated for all individual slabs using a timing window of 40 ns. Gaussian fitting was performed and the FWHM timing resolution was obtained.

3 Results

3.1 Flood histograms

The flood histograms of the four detectors are shown in Fig. 6. The flood histograms show the *x* and *y* positions of the interactions of the gamma rays with the detectors, where the grayscale value of the color bar represents the number of interactions occurring at these positions. The profiles through the middle of each flood histogram are also shown in Fig. 6. The average peak-to-valley ratios of the four detectors were 3.03 ± 0.96, 4.67 ± 1.29, 5.04 ± 1.44, and 2.58 ± 0.85, respectively. All slabs were clearly resolved for detectors 1–3 using 0.96 mm-thick slabs. As shown in the

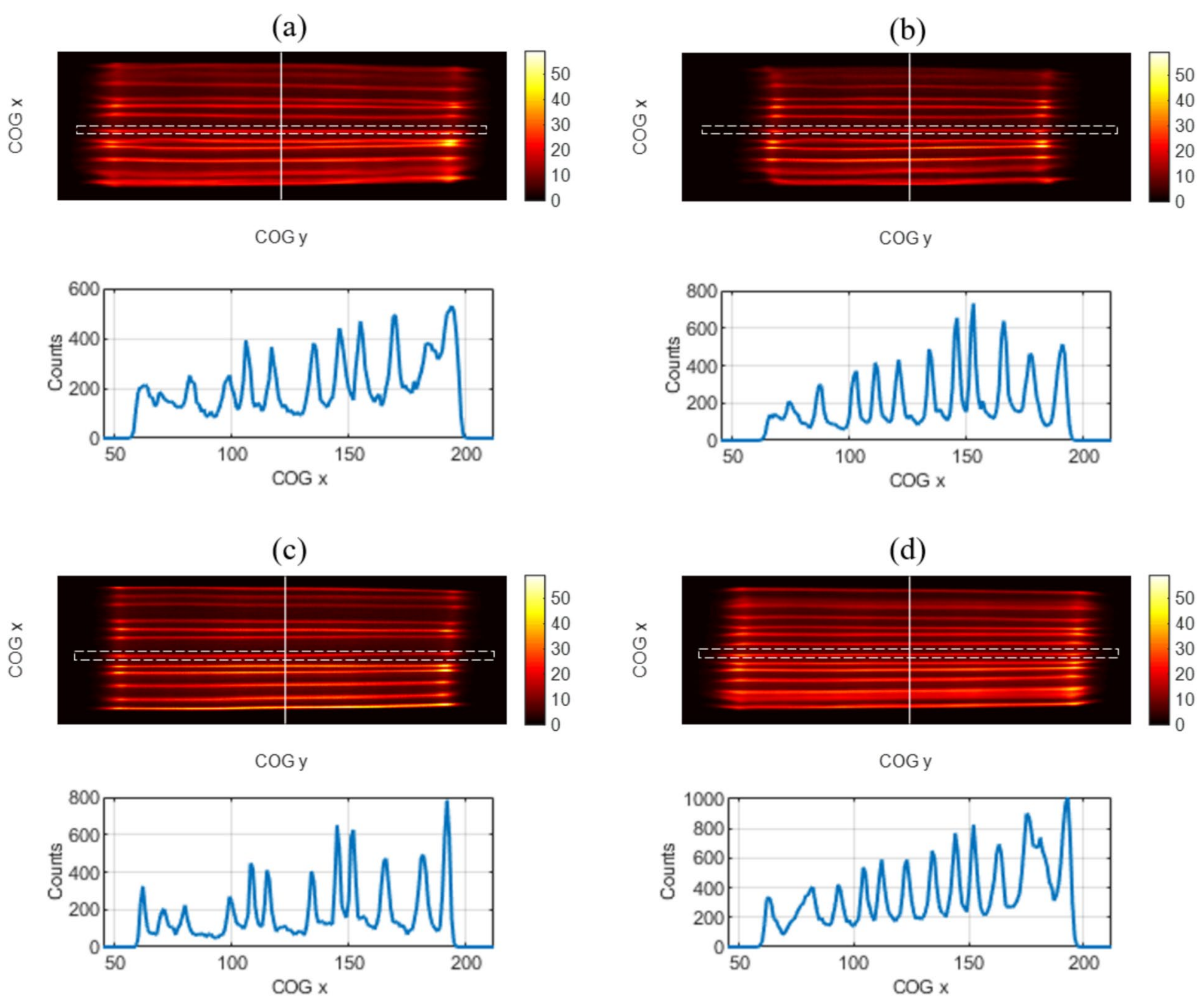

Fig. 6 (Color online) Flood histograms obtained using the COG method with an energy window of 350 – 650 keV for detectors **a** 1, **b** 2, **c** 3, and **d** 4. The slab between the two white dashed lines was selected from each detector to plot the energy spectra, *y* profiles, and DOI profiles

flood histogram, along the x coordinates of the detector, slab identification was best achieved in detector 3, which used the ESR reflector. The second and third slabs near the edges could not be clearly resolved for detector 4 using 0.81 mm-thick slabs. The positions of the cuts in the lightguide likely need to be further optimized. Black painting of the two end and front surfaces of the slabs reduced the scintillation photon reflection at those surfaces and mainly resulted in longer flood histograms in the monolithic direction, implying a better y position resolution, while the slab identification was almost unchanged.

3.2 Energy resolution

The energy spectra of the middle slabs of the four detectors measured at the five DOIs are shown in Fig. 7. Detector 3, which used a specular ESR reflector, had the lowest light output; however, the photopeak amplitudes did not change with the depth. The other three detectors, which used the diffusive $BaSO_4$ reflector, had a much higher light output; however, the photopeak amplitude changed significantly with the depth. A depth-dependent energy calibration is required for these detectors. The average energy resolutions of detectors 1 and 4 measured at the 27×5 (y, z) positions are listed in Table 2. Average energy resolutions of 17.4% and 17.6% were achieved for the two detectors, implying that the thickness of the slab had a small effect on the energy resolution. The average energy resolutions of the four detectors measured at the 27 y positions along the middle DOI are listed in Table 3. The average energy resolutions for detectors 1–4 were 15.8%, 14.7%, 15.8%, and 16.4%, respectively. Detector 2 (without black paint) exhibited the best energy resolution because the black paint absorbed some scintillation photons, thereby degrading the energy resolutions of the other three detectors.

3.3 Spatial resolution in the monolithic direction

The curves of the peak positions of the COG and squared COG algorithms for different y irradiation positions measured at three depths are shown in Fig. 8 for detectors 1 and 4. The curves were linear at the middle of the detectors and became nonlinear at both ends owing to scintillation photon reflection and truncation. The nonlinearity decreased as the depth increased. Nonlinearity increases the challenge of detector calibration and degrades the spatial resolution

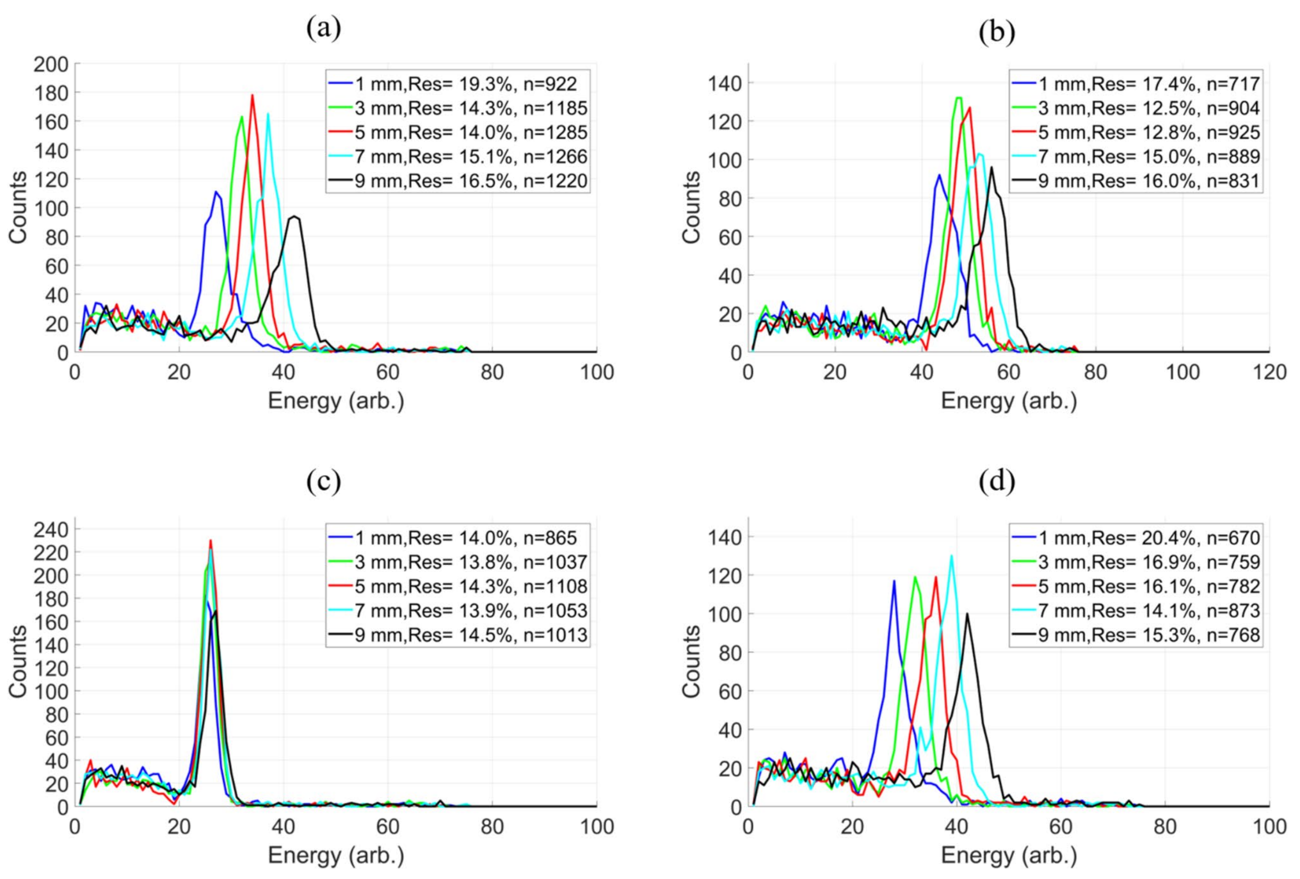

Fig. 7 (Color online) Energy spectra of the middle slabs, as shown in Fig. 6, measured at the middle y position and various DOI positions for detectors **a** 1, **b** 2, **c** 3, and **d** 4. n is the number of events of each curve

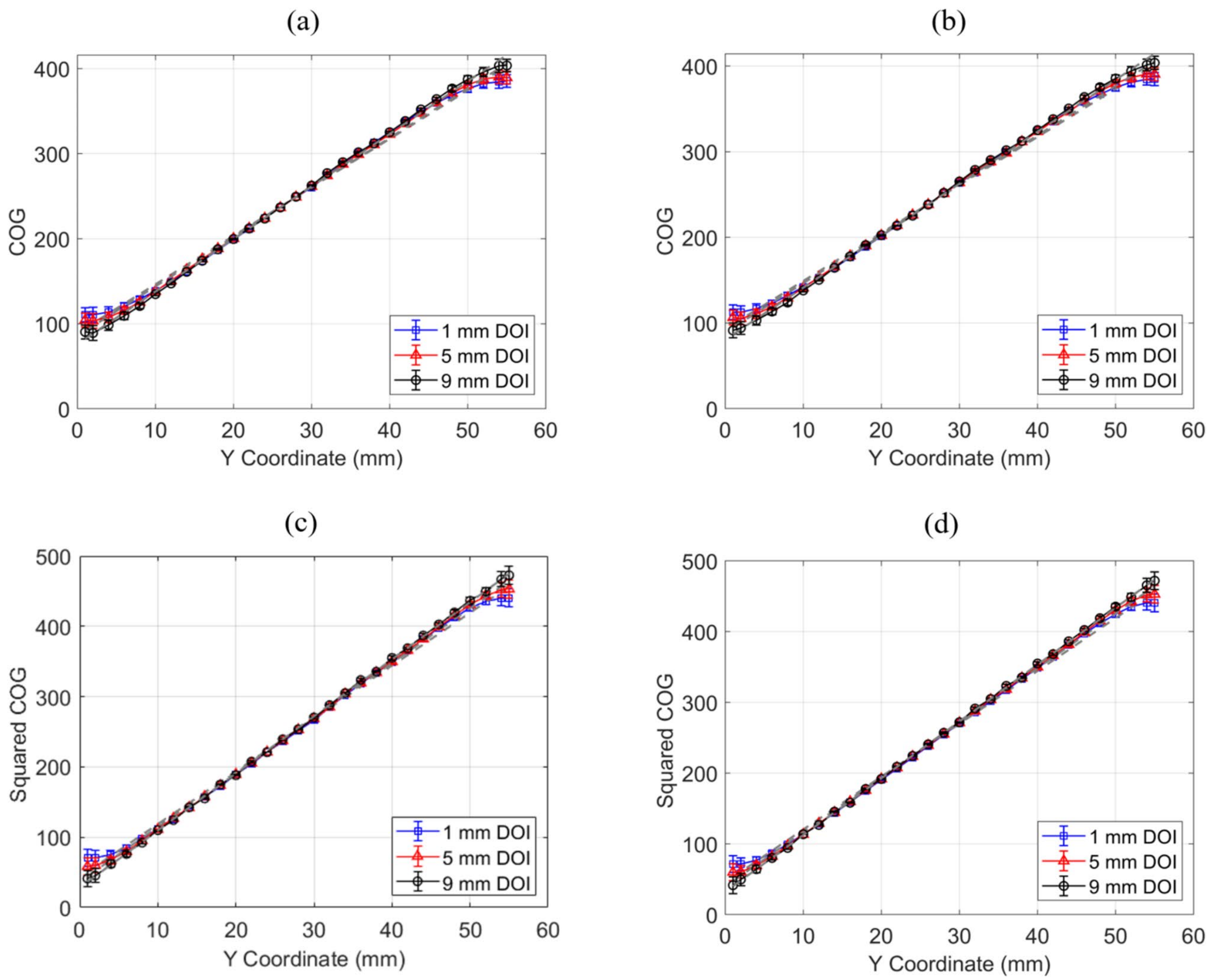

Fig. 8 (Color online) Peak positions of the measured y histograms vs. the true y irradiation positions. **a** Detector 1, COG method, **b** detector 4, COG method, **c** detector 1, squared COG method, and **d** detector 4, squared COG method. The number of events for each position was ~1000

in the monolithic direction. The curves were similar for different slabs of the detector (data not shown). Figure 9 shows the y profiles of the 27 different y positions and two DOIs of detector 1 obtained using the two positioning methods. The horizontal coordinates of the y profiles were converted into mm using the curves shown in Fig. 8. For both methods, the resolvability of the profiles deteriorated more toward both ends owing to the edge effect. To demonstrate the effects of the positioning methods and depths on the y spatial resolution more clearly, y profiles of a DOI of 5 mm and y of 42 mm obtained using the COG and squared COG methods, and y profiles of DOIs of 1 and 5 mm and y of 42 mm obtained using the squared COG method are shown in Fig. 9e and f, respectively.

Figure 10 shows the spatial resolutions of all irradiation positions of detectors 1 and 4 using the COG and squared COG methods. For both methods, the y spatial resolution improved as the DOI moved toward the SiPM. The y spatial resolution degraded as the y position moved toward both ends owing to edge effects. At the DOI near the SiPM, a variation in the y spatial resolution with changes in the y positions was observed because of the gaps between the SiPM pixels and inactive areas at the edge of the SiPM pixels. The squared COG method showed a better y spatial resolution than the COG method. As shown in Table 2, the y spatial resolutions averaged over the entire detectors were 1.68 ± 0.29 and 1.67 ± 0.27 mm for detectors 1 and 4, respectively. As shown in Table 3, the average y spatial resolutions measured at a depth of 5 mm were 1.66 ± 0.16, 1.87 ± 0.31, 1.71 ± 0.26, and 1.67 ± 0.14 mm for detectors 1 to 4, respectively.

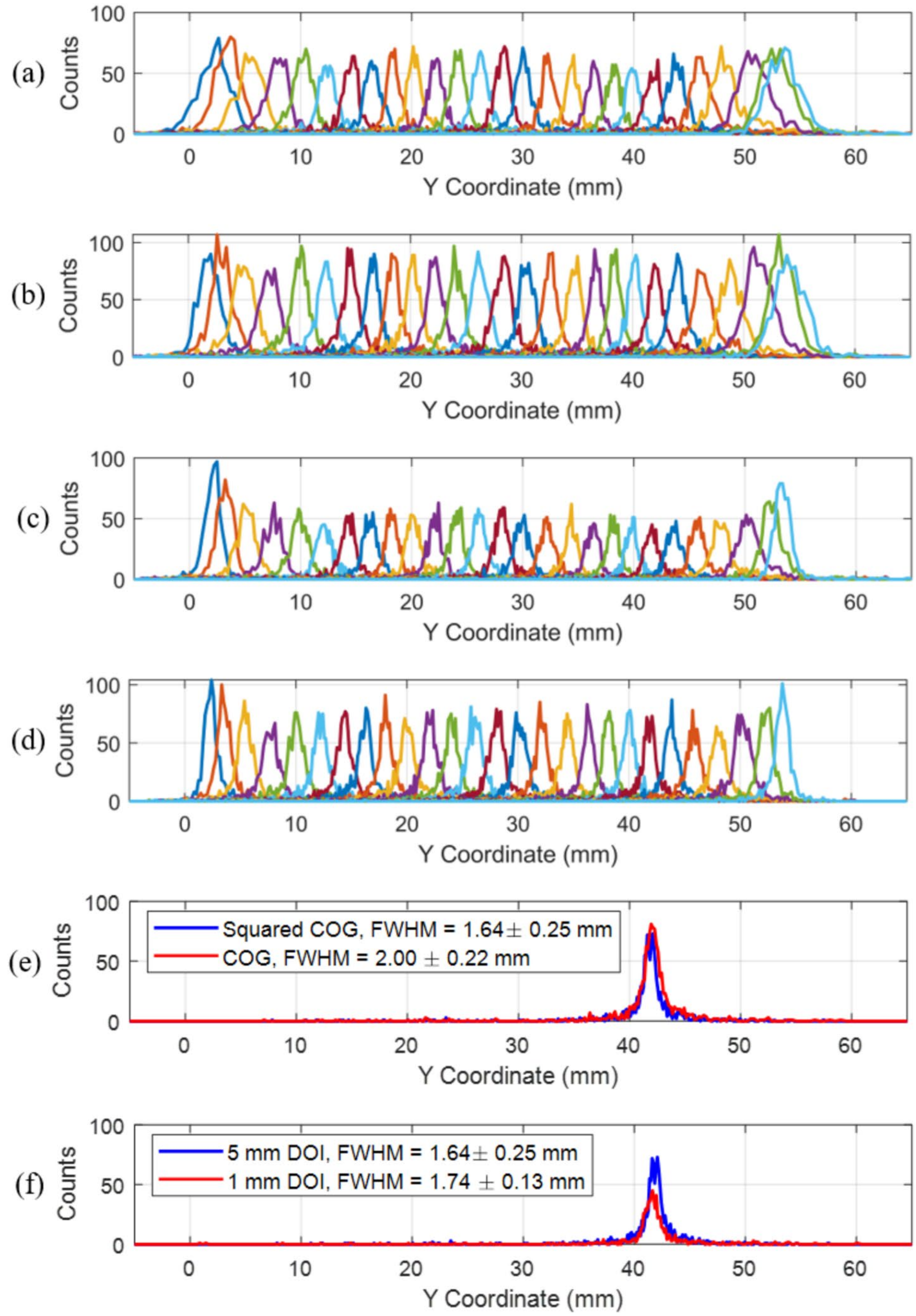

Fig. 9 (Color online) The *y* profiles in mm for one middle slab of detector 1, as shown in Fig. 6: **a** COG method, 1 mm DOI, 27 *y* positions, **b** COG method, 5 mm DOI, 27 *y* positions, **c** squared COG method, 1 mm DOI, 27 *y* positions, **d** squared COG method, 5 mm DOI, 27 *y* positions, **e** both methods, 5 mm DOI, 42 mm *y*, and **f** squared COG method, 1 and 5 mm DOIs, 42 mm *y*. The number of events for each position was ~1000

3.4 DOI resolution

Figure 11 shows the DOI profiles of the four detectors measured at the center *y* position (28 mm). The DOI resolution degraded significantly as the DOI moved away from the SiPM. This is because the change in the scintillation photon distribution width with the DOI decreased as the DOI moved farther from the SiPM. Figure 12 shows the DOI resolutions at all irradiation positions for detectors 1 and 4. The DOI resolution also degraded toward both ends of the detector owing to the edge effect. The average DOI resolution results are summarized in Tables 2 and 3. The DOI resolutions averaged over the entire detectors were 2.14 ± 0.76 and 2.28 ± 0.67 mm for detectors 1 and 4, respectively. Detector 2, with unpainted surfaces at the front and both ends, provided the worst DOI resolution of 3.41 ± 2.80 mm averaged over the five DOIs along the center *y*. The other three detectors, with black paint on these surfaces, provided a similar DOI resolution of ~1.9 mm averaged over the five DOIs along the center *y*.

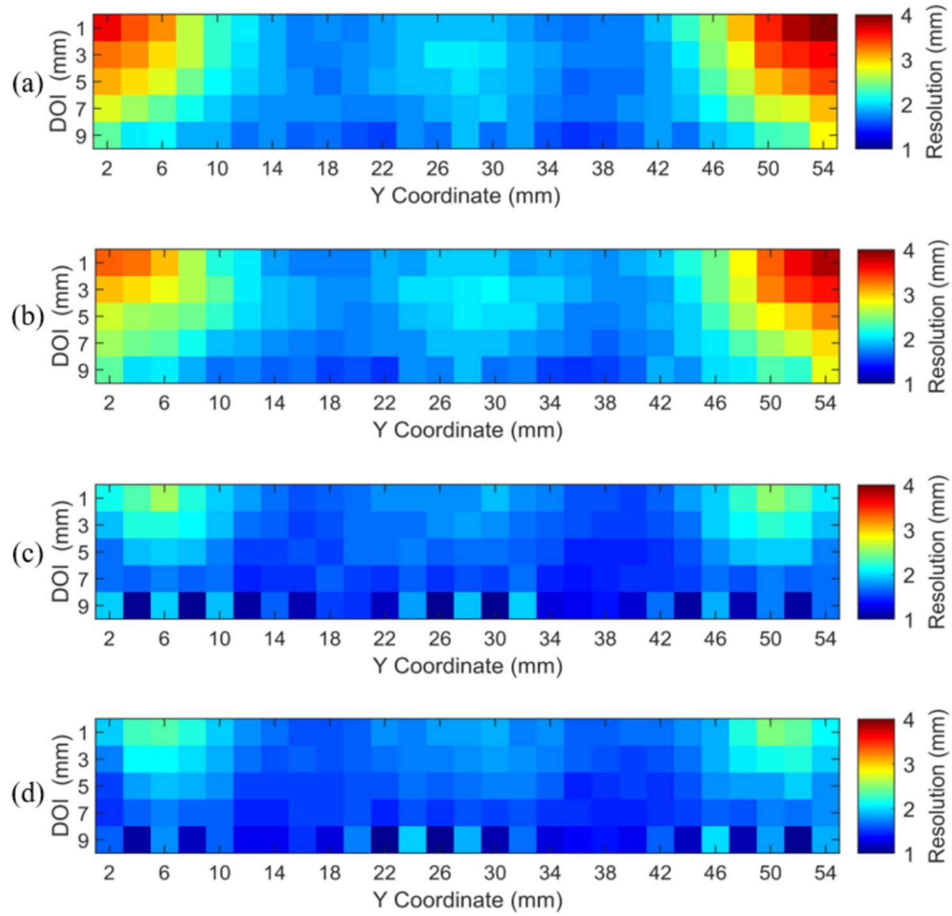

Fig. 10 (Color online) The *y* spatial resolutions of all irradiation positions: **a** detector 1, COG method, **b** detector 4, COG method, **c** detector 1, squared COG method, and **d** detector 4, squared COG method. The counts of each irradiation position were ~1000 per slab

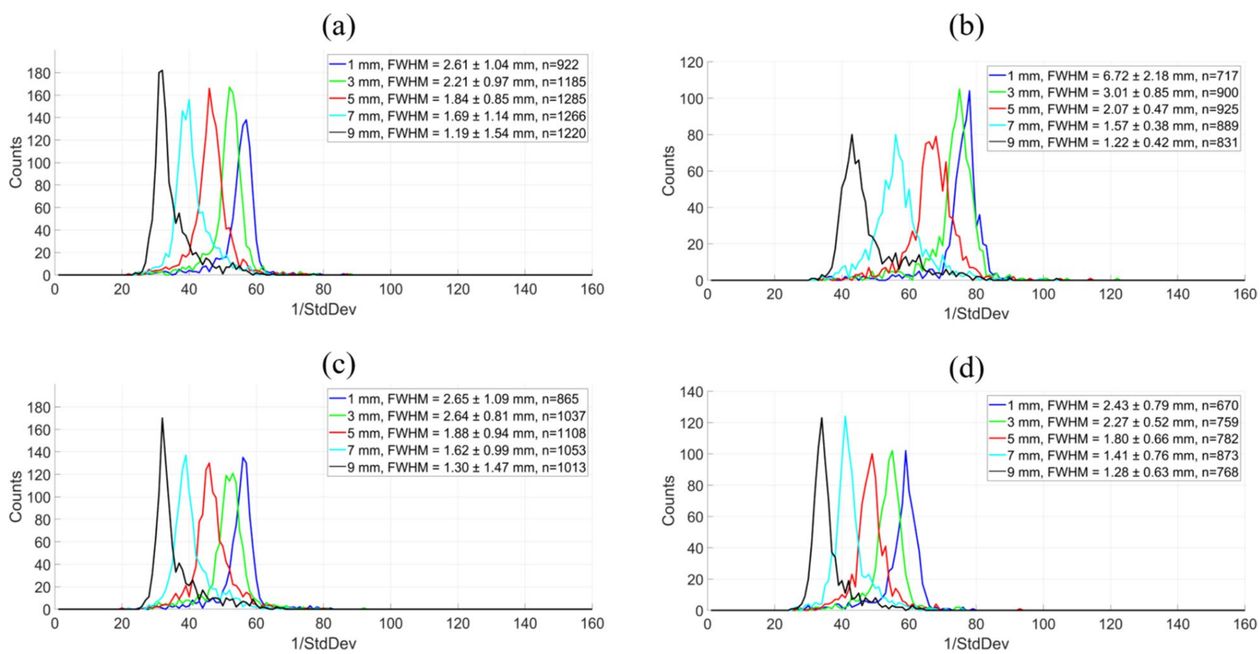

Fig. 11 (Color online) DOI profiles of the middle slabs, as shown in Fig. 6, measured for a *y* position of 28 mm and depths of 1, 3, 5, 7, and 9 mm for detectors **a** 1, **b** 2, **c** 3 and **d** 4. *n* is the number of events of each curve

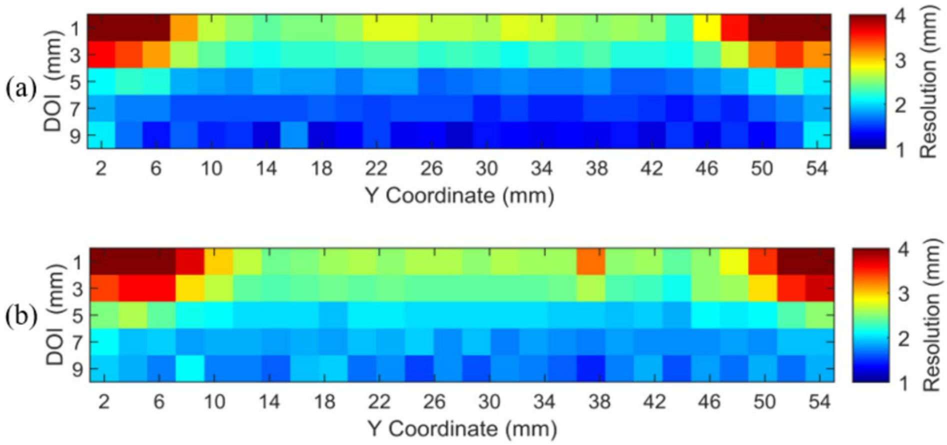

Fig. 12 (Color online) DOI resolutions at all irradiated positions of detectors **a** 1 and **b** 4. The number of events for each irradiation position was ~1000 per slab

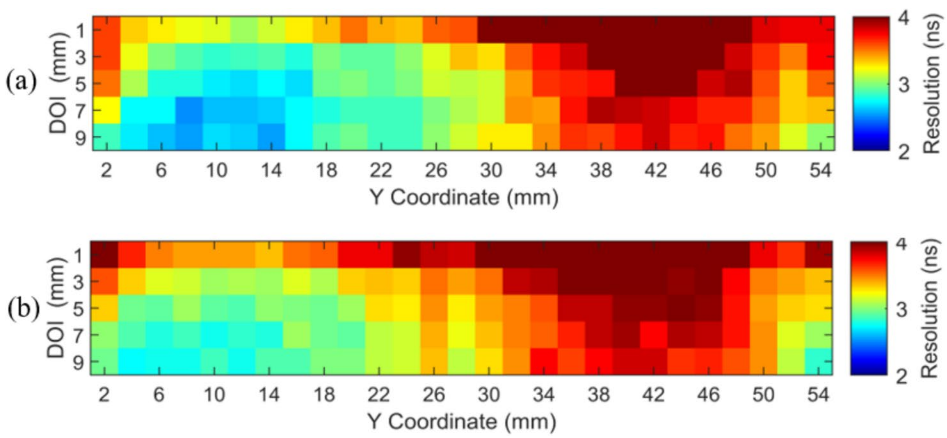

Fig. 13 (Color online) Timing resolutions at all irradiated positions of detectors **a** 1 and **b** 4. The number of events of each irradiation position was ~1000 per slab

Table 2 Summary of the results of detectors 1 and 4 averaged over 27×5 irradiation positions

Detectors	1	4
y resolution, COG (mm)	2.15 ± 0.57	2.12 ± 0.50
y resolution, squared COG (mm)	1.68 ± 0.29	1.67 ± 0.27
DOI resolution (mm)	2.14 ± 0.76	2.28 ± 0.67
Energy resolution (%)	17.4 ± 2.4	17.6 ± 2.0
Timing resolution (ns)	3.34 ± 0.49	3.47 ± 0.45

3.5 Timing resolution

Figure 13 shows the timing resolutions of detectors 1 and 4. The average timing resolutions of the four detectors are listed in Tables 2 and 3. The timing resolutions of the four detectors were similar. The poor timing resolution results in this work resulted from the unoptimized timing pick-off circuit rather than the semi-monolithic scintillator detector because a timing resolution of < 600 ps has been obtained

Table 3 Summary of the results for all four detectors

Detectors	1	2	3	4
y resolution, COG (mm)	2.15 ± 0.57	2.65 ± 0.80	2.45 ± 0.69	2.13 ± 0.42
y resolution, squared COG (mm)	1.66 ± 0.16	1.87 ± 0.31	1.71 ± 0.26	1.67 ± 0.14
DOI resolution (mm)	1.92 ± 0.51	3.41 ± 2.80	1.94 ± 0.47	1.87 ± 0.47
Energy resolution (%)	15.8 ± 2.2	14.7 ± 1.3	15.8 ± 0.9	16.4 ± 1.3
Timing resolution (ns)	3.29 ± 0.53	3.09 ± 0.47	3.39 ± 0.50	3.38 ± 0.48

The *y* spatial resolution and energy resolution were averaged over the 27 irradiation positions along the center DOI. The DOI resolution was averaged over the five irradiation positions along the center *y* for a small semi-monolithic detector using nuclear instrument module electronics [26].

4 Discussion and conclusions

In this study, the performances of four PET detector modules consisting of semi-monolithic LYSO slabs with different surface treatments, inter-slab reflectors, and slab thicknesses were evaluated using signal processing electronics developed in our laboratory. To the best of our knowledge, these are the longest (56 mm) and thinnest (0.81 mm) semi-monolithic scintillator PET detectors measured to date. Semi-monolithic scintillator PET detectors using ESR and $BaSO_4$ reflectors were compared for the first time.

Using a lightguide with grooves near both ends, clear slab identification was attained for the three detectors using LYSO slabs of 0.96 mm thickness. The second and third slabs at the edges could not be clearly identified by the detector using 0.81 mm-thick LYSO slabs. The groove positions in the lightguide will be optimized in the future.

Black paint treatment of the two end and front surfaces degraded the energy resolution but improved both the spatial resolution in the monolithic direction and DOI resolution. The energy resolution degraded from 14.7% to 15.8%. The spatial resolution in the monolithic direction improved from 2.65 to 2.15 mm for the COG method, and from 1.87 to 1.66 mm for the squared COG method. The DOI resolution improved from 3.41 to 1.92 mm. Overall, black paint treatment of the crystal surfaces improved the performance of the semi-monolithic PET detectors.

Although the detector using an ESR as the inter-slab reflector provided the lowest light output, the photopeak amplitude remained almost unchanged with the DOI, making the energy calibration of the detector much easier. The detector using the ESR reflector provided clearer individual slab identification in the flood histogram, with similar spatial resolution in the monolithic direction, DOI resolution, and energy resolution. Overall, the ESR is a better inter-slab reflector than the $BaSO_4$ reflector.

In this study, the squared COG positioning method was compared with the traditional COG method. The squared COG method assigns more weight to SiPM column signals with high amplitudes and improves the spatial resolution in the monolithic direction by ~30% by reducing the effect of signals with poor signal-to-noise ratios. The squared COG method can also be easily implemented in modern PET electronics.

Both pixelated and monolithic scintillator detectors have been used in the development of high-resolution small-animal and organ-specific PET scanners. Semi-monolithic detectors present a suitable alternative to these detectors because the edge effect is smaller than that of monolithic detectors, and the DOI can be measured with a single-ended readout compared with pixelated scintillator detectors that require a dual-ended readout or more complex detector designs. The cost of the semi-monolithic scintillator is lower than that of the pixelated detector but higher than that of the monolithic detector. In the future, an SiPM array with smaller gaps between pixels will be used, crystal surface treatments will be further optimized, and a machine-learning-based positioning algorithm will be developed to improve the resolutions in both the monolithic and DOI directions. Semi-monolithic scintillator detectors with thinner slabs and ESR reflectors will be evaluated. Advanced signal processing techniques will be studied to improve the timing resolution of the detector and explore the possibility of using semi-monolithic scintillator detectors in time-of-flight PET scanners.

In summary, the long semi-monolithic scintillator detectors optimized in this work provide clear identification of LYSO slabs of 0.96 and 0.81 mm thick, a spatial resolution in the monolithic direction of ~1.7 mm using the squared COG method, a DOI resolution of ~1.9 mm, and energy resolutions of ~16%. Because the irradiation beam width of ~1 mm is not subtracted from the measured results, the true spatial resolution in the monolithic direction and DOI resolution are even better. Based on the performance achieved, these detectors can be used to develop high-performance small-animal and organ-specific PET scanners in the future.

Author contributions All authors participated in the conception and design of the research. Material preparation, data collection, and analysis were performed by Samuel Mungai Kinyanjui and Kuang Zhong-Hua Kuang. Funding acquisition was performed by Zhong-Hua Kuang and Yong-Feng Yang. The initial draft was written by Samuel Mungai Kinyanjui, and all authors read and provided suggestions on the revisions of the manuscript. The manuscript was then revised by Yong-Feng Yang and the final version of the manuscript was approved by all authors.

Data availability The data that support the findings of this study are openly available in Science Data Bank at https://cstr.cn/31253.11.sciencedb.35988 and https://doi.org/10.57760/sciencedb.35988

Declarations

Conflict of interest The authors declare that they have no conflict of interest.

References

1. S.R. Cherry, T. Jones, J.S. Karp et al., Total-Body PET: maximizing sensitivity to create new opportunities for clinical research

and patient care. J. Nucl. Med. **59**, 3–12 (2018). https://doi.org/10.2967/jnumed.116.184028
2. S. Vandenberghe, P. Moskal, J.S. Karp, State of the art in total body PET. EJNMMI Phys. **7**, 35 (2020). https://doi.org/10.1186/s40658-020-00290-2
3. V. Bettinardi, I. Castiglioni, E. De Bernardi et al., PET quantification: strategies for partial volume correction. Clin. Transl. Imaging **2**, 199–218 (2014). https://doi.org/10.1007/s40336-014-0066-y
4. Y. Yang, J. Bec, J. Zhou et al., A prototype high-resolution small-animal PET scanner dedicated to mouse brain imaging. J. Nucl. Med. **57**, 1130–1135 (2016). https://doi.org/10.2967/jnumed.115.165886
5. R.S. Miyaoka, A.L. Lehnert, Small animal PET: a review of what we have done and where we are going. Phys. Med. Biol. **65**, 24TR04 (2020). https://doi.org/10.1088/1361-6560/ab8f71
6. J. Du, T. Jones, Technical opportunities and challenges in developing total-body PET scanners for mice and rats. EJNMMI Phys. **10**, 2 (2023). https://doi.org/10.1186/s40658-022-00523-6
7. A. Verger, A. Kas, J. Darcourt et al., PET imaging in neuro-oncology: an update and overview of a rapidly growing area. Cancers **14**, 1103 (2022). https://doi.org/10.3390/cancers14051103
8. C. Catana, Development of dedicated brain PET imaging devices: recent advances and future perspectives. J. Nucl. Med. **60**, 1044–1052 (2019). https://doi.org/10.2967/jnumed.118.217901
9. S. Vandenberghe, E. Mikhaylova, E. D'Hoe et al., Recent developments in time-of-flight PET. EJNMMI Phys. **3**, 3 (2016). https://doi.org/10.1186/s40658-016-0138-3
10. J. Van Sluis, J. De Jong, J. Schaar et al., Performance characteristics of the digital biograph vision PET/CT system. J. Nucl. Med. **60**, 1031–1036 (2019). https://doi.org/10.2967/jnumed.118.215418
11. L. Eriksson, K. Wienhard, M. Eriksson et al., The ECAT HRRT: NEMA NEC evaluation of the HRRT system, the new high-resolution research tomograph. IEEE Trans. Nucl. Sci. **49**, 2085–2088 (2002). https://doi.org/10.1109/TNS.2002.803784
12. N. Inadama, H. Murayama, M. Hamamoto et al., 8-layer DOI encoding of 3-dimensional crystal array. IEEE Trans. Nucl. Sci. **53**, 2523–2528 (2006). https://doi.org/10.1109/TNS.2006.882795
13. Y. Yang, P.A. Dokhale, R.W. Silverman et al., Depth of interaction resolution measurements for a high resolution PET detector using position sensitive avalanche photodiodes. Phys. Med. Biol. **51**, 2131–2142 (2006). https://doi.org/10.1088/0031-9155/51/9/001
14. Z. Kuang, X. Wang, N. Ren et al., Design and performance of SIAT aPET: a uniform high-resolution small animal PET scanner using dual-ended readout detectors. Phys. Med. Biol. **65**, 235013 (2020). https://doi.org/10.1088/1361-6560/abbc83
15. Z. Gu, R. Taschereau, N.T. Vu et al., Performance evaluation of HiPET, a high sensitivity and high resolution preclinical PET tomograph. Phys. Med. Biol. **65**, 045009 (2020). https://doi.org/10.1088/1361-6560/ab6b44
16. P. Bruyndonckx, S. Leonard, S. Tavernier et al., Neural network-based position estimators for PET detectors using monolithic LSO blocks. IEEE Trans. Nucl. Sci. **51**, 2520–2525 (2004). https://doi.org/10.1109/TNS.2004.835782
17. M.C. Maas, D.J. van der Laan, D.R. Schaart et al., Experimental characterization of monolithic-crystal small animal PET detectors read out by APD arrays. IEEE Trans. Nucl. Sci. **53**, 1071–1077 (2006). https://doi.org/10.1109/TNS.2006.873711
18. M. Balcerzyk, G. Kontaxakis, M. Delgado et al., Initial performance evaluation of a high resolution Albira small animal positron emission tomography scanner with monolithic crystals and depth-of-interaction encoding from a user's perspective. Meas. Sci. Technol. **20**, 104011 (2009). https://doi.org/10.1088/0957-0233/20/10/104011
19. S. Krishnamoorthy, E. Blankemeyer, P. Mollet et al., Performance evaluation of the MOLECUBES β-CUBE a high spatial resolution and high sensitivity small animal PET scanner utilizing monolithic LYSO scintillation detectors. Phys. Med. Biol. **63**, 155013 (2018). https://doi.org/10.1088/1361-6560/aacec3
20. W. Gsell, C. Molinos, C. Correcher et al., Characterization of a preclinical PET insert in a 7 tesla MRI scanner: beyond NEMA testing. Phys. Med. Biol. **65**, 245016 (2020). https://doi.org/10.1088/1361-6560/aba08c
21. G. Borghi, V. Tabacchini, D.R. Schaart, Towards monolithic scintillator based TOF-PET systems: practical methods for detector calibration and operation. Phys. Med. Biol. **61**, 4904–4928 (2016). https://doi.org/10.1088/0031-9155/61/13/4904
22. M. Stockhoff, R.V. Holen, S. Vandenberghe, Optical simulation study on the spatial resolution of a thick monolithic PET detector. Phys. Med. Biol. **64**, 195003 (2019). https://doi.org/10.1088/1361-6560/ab3b83
23. G. Borghi, V. Tabacchini, S. Seifert et al., Experimental validation of an efficient fan-beam calibration procedure for k-nearest neighbor position estimation in monolithic scintillator detectors. IEEE Trans. Nucl. Sci. **62**, 57–67 (2015). https://doi.org/10.1109/TNS.2014.2375557
24. Y.H. Chung, S.J. Lee, C.H. Baek et al., New design of a quasi-monolithic detector module with DOI capability for small animal pet. Nucl. Instrum. Meth. A. **593**, 588–591 (2008). https://doi.org/10.1016/j.nima.2008.05.059
25. Y.H. Chung, C.H. Baek, S.J. Lee et al., Preliminary experimental results of a quasi-monolithic detector with DOI capability for a small animal PET. Nucl. Instrum. Meth. A. **621**, 590–594 (2010). https://doi.org/10.1016/j.nima.2010.04.039
26. X. Zhang, X. Wang, N. Ren et al., Performance of a SiPM based semi-monolithic scintillator PET detector. Phys. Med. Biol. **62**, 7889–7904 (2017). https://doi.org/10.1088/1361-6560/aa898a
27. Z. Kuang, X. Wang, C. Li et al., Performance of a high-resolution depth encoding PET detector using barium sulfate reflector. Phys. Med. Biol. **62**, 5945–5958 (2017). https://doi.org/10.1088/1361-6560/aa71f3
28. X. Zhang, X. Wang, N. Ren et al., Performance of long rectangular semi-monolithic scintillator PET detectors. Med. Phys. **46**, 1608–1619 (2019). https://doi.org/10.1002/mp.13432
29. Y. Kuhl, F. Mueller, S. Naunheim et al., A finely segmented semi-monolithic detector tailored for high-resolution PET. Med. Phys. **51**, 3421–3436 (2024). https://doi.org/10.1002/mp.16928
30. N. Cucarella, J. Barrio, E. Lamprou et al., Timing evaluation of a PET detector block based on semi-monolithic LYSO crystals. Med. Phys. **48**, 8010–8023 (2021). https://doi.org/10.1002/mp.15318
31. C. Zhang, X. Wang, M. Sun et al., A thick semi-monolithic scintillator detector for clinical PET scanners. Phys. Med. Biol. **66**, 065023 (2021). https://doi.org/10.1088/1361-6560/abe761
32. F. Mueller, S. Naunheim, Y. Kuhl et al., A semi-monolithic detector providing intrinsic DOI-encoding and sub-200 ps CRT TOF-capabilities for clinical PET applications. Med. Phys. **49**, 7469–7488 (2022). https://doi.org/10.1002/mp.16015
33. M. Freire, J. Barrio, N. Cucarella et al., Position estimation using neural networks in semi-monolithic PET detectors. Phys. Med. Biol. **67**, 245011 (2022). https://doi.org/10.1088/1361-6560/aca389
34. A. Iborra, A.J. González, A.G. Montoro et al., Ensemble of neural networks for 3D position estimation in monolithic PET detectors. Phys. Med. Biol. **64**, 195010 (2019). https://doi.org/10.1088/1361-6560/ab3b86
35. Z. Kuang, Z. Sang, N. Ren et al., Development and performance of SIAT bPET: a high-resolution and high-sensitivity MR-compatible brain PET scanner using dual-ended readout detectors.

Eur. J. Nucl. Med. Mol. Imaging **51**, 346–357 (2024). https://doi.org/10.1007/s00259-023-06458-z

36. J. Lu, L. Zhao, K. Chen et al., Real-time FPGA-based digital signal processing and correction for a small animal PET. IEEE Trans. Nucl. Sci. **66**, 1287–1295 (2019). https://doi.org/10.1109/TNS.2019.2908220
37. L. Zhao, C. Ma, S. Chu et al., Prototype of the readout electronics for WCDA in LHAASO. IEEE Trans. Nucl. Sci. **64**, 1367–1373 (2017). https://doi.org/10.1109/TNS.2017.2693296
38. P. Deng, L. Zhao, J. Lu et al., Prototype design of singles processing unit for the small animal PET. J. Instrum. **13**, T05007 (2018). https://doi.org/10.1088/1748-0221/13/05/T05007
39. K. Chen, L. Zhao, L. Zhang, et al., Testing of singles processing unit for a brain PET. In: 2021 IEEE Nuclear Science Symposium and Medical Imaging Conference (NSS/MIC), pp. 1–3 (2021). https://doi.org/10.1109/NSS/MIC44867.2021.9875447
40. D. Schug, J. Wehner, B. Goldschmidt et al., Data processing for a high resolution preclinical PET detector based on Philips DPC digital SiPMs. IEEE Trans. Nucl. Sci. **62**, 669–678 (2015). https://doi.org/10.1109/TNS.2015.2420578

Authors and Affiliations

Samuel Mungai Kinyanjui[1,2] · Zhonghua Kuang[1,3] · Zheng Liu[1] · Ning Ren[1] · Yongfeng Yang[1]

✉ Yongfeng Yang
yf.yang@siat.ac.cn

[1] Paul C. Lauterbur Research Center for Biomedical Imaging, Shenzhen Institutes of Advanced Technology, Chinese Academy of Sciences, Shenzhen 518055, China

[2] Shenzhen College of Advanced Technology, University of Chinese Academy of Sciences, Shenzhen 518055, China

[3] Microelectronics and Optoelectronics Technology Key Laboratory of Hunan Higher Education, School of Physics and Electronic Electrical Engineering, Xiangnan University, Chenzhou 423000, China